Materials Advances

ROYAL SOCIETY OF CHEMISTRY

PAPER

View Article Online
View Journal | View Issue

Cite this: *Mater. Adv.*, 2026, 7, 5336

Carbon nanotube incorporated magnetic biochar derived from water hyacinth for chromium removal from tannery effluent

M. Hedayet Ullah[ab] and Mohammad Jellur Rahman *[a]

This study presents a magnetically separable, biochar-supported nanocomposite adsorbent for efficient removal of chromium (Cr) from tannery wastewater. Biochar is derived from stems of water hyacinth (WH), an invasive aquatic plant, and modified with 1 wt% carbon nanotubes (CNTs) and 5 wt% Co–Zn ferrite nanoparticles. The CNT and Co–Zn ferrite incorporated biochar (CNT-CZB) nanocomposite exhibits a mesoporous structure with a rough surface morphology. The CNT-CZB achieved a maximum adsorption capacity of ~81 mg g^{-1} for the synthetic solution and ~101 mg g^{-1} for real tannery wastewater. Adsorption is pH-dependent, enhanced at higher temperature and Cr concentration, and rapid in the initial stage. Adsorption kinetics and isotherms suggest chemical processes primarily govern Cr adsorption with mixed monolayer and multilayer adsorption behavior. Thermodynamic studies reveal that the process is spontaneous and thermodynamically favorable. Key adsorption mechanisms include electrostatic interactions, complexation with oxygen-containing functional groups, and the reduction of Cr from hexavalent to trivalent states. Statistical optimization using Box–Behnken design reveals that the adsorption capacity is predominantly controlled by the initial Cr concentration, followed by pH and reaction time. This research demonstrates a dual-benefit solution by converting problematic WH plants into sustainable and value-added materials while reducing water pollution through Cr adsorption.

Received 9th March 2026,
Accepted 22nd April 2026

DOI: 10.1039/d6ma00330c

rsc.li/materials-advances

1. Introduction

Rapid industrial growth has made wastewater management more challenging, causing significant harm to the aquatic environment and posing substantial threats to global environmental sustainability. Industrial wastewater contains hazardous contaminants, including heavy metals (HMs), organic solvents, dyes, antibiotics, *etc.* which are directly discharged into the surface water. The concentration of HMs such as chromium (Cr) in various ecosystems has exceeded their acceptable safety levels because of the negligent practice of pollutant-loaded waste disposal.[1] Due to high solubility in water, non-degradable nature, and toxicity of Cr, it can quickly enter the food chain and cause severe health damage, even cancer in severe and chronic cases.[2,3]

Cr is a transition metal used extensively in the tannery, textile, electroplating, and other chemical industries due to its distinctive characteristics, like corrosion resistance, thermal stability, hardness, and colorants.[4] In nature, Cr has two oxidation states: Cr(III) and Cr(VI), among which compounds of hexavalent Cr are more reactive, water-soluble, and toxic than trivalent Cr.[5] Traditional water treatment methods, including precipitation, ion exchange, electrolysis, membrane filtration, biological processes, and adsorption, have been employed to eliminate Cr from aqueous solutions.[6–8] Among these, adsorption is a promising technique because of its safety, high efficiency, ease of operation, and cost-effectiveness.[9] A diverse range of adsorbents, such as activated carbon, graphene oxide, carbon nanotubes (CNTs), chitosan, agricultural waste, zeolites, biochar, *etc.* have been employed for HMs removal.[10,11]

The adsorption efficiency of adsorbents is strongly influenced by their physicochemical properties, including specific surface area, pore network, surface functional groups, and the interaction mechanisms with HM ions.[12] In recent years, CNTs have gained significant attention as an adsorbent in water treatment due to their lightweight, high surface area, and chemical stability.[13] CNTs are cylindrical, composed of rolled-up graphene sheets, and exhibit sp^2 hybridization.[14] Previous studies have confirmed a strong binding affinity between CNTs and the HMs ions.[15,16] However, the potential applications of CNTs in environmental problems are limited because pristine CNTs are insoluble in water and tend to aggregate into bundles.

[a] *Department of Physics, Bangladesh University of Engineering and Technology, Dhaka 1000, Bangladesh. E-mail: mjrahman@phy.buet.ac.bd*
[b] *Department of Physics, Bangladesh University of Textiles, Dhaka 1208, Bangladesh. E-mail: hedayet@phy.butex.edu.bd*

Several studies have investigated improving the dispersibility of CNTs by surface functionalization with oxygen- and sulfur-containing functional groups.[17,18] These functional groups reduced Cr(VI) to its less toxic form, Cr(III), and surface complexation of metal ions by these groups is considered one of the primary mechanisms for HMs adsorption by carbon-based nanocomposites.[19]

CNTs can be loaded onto low-cost, eco-friendly carriers such as biochar to prevent aggregation. Biochar is a carbon-rich material produced by pyrolysis in an oxygen-limited environment derived from agricultural biomass. The positive impact of biochar in wastewater treatment has already been recognized.[20–22] Thus, combining traditional biochar with functionalized carbon nanotubes (f-CNTs) can produce a high-performance hybrid adsorbent for removing Cr from wastewater.

Additionally, separating powder biochar-based adsorbents from aqueous solutions remains a significant challenge and can lead to secondary pollution. To address this issue, Co–Zn spinel ferrite is introduced into the hybrid nanocomposite to make it a magnetic material. Spinel ferrite nanoparticles offer easy magnetic separation and more active sites, making them excellent adsorbents for wastewater treatment.

Statistical approaches in experimental design are crucial for determining the combined effect of multiple variables in a process. Box–Behnken design (BBD), a response surface methodology (RSM), is a statistical tool used to design experiments and analyze the influence of several independent factors.[23] BBD requires fewer experimental runs and analyzes the interaction among multiple variables.[24] The least squares fitting is applied to estimate the coefficients of the polynomial equation that best describes the relationship between the variables and the response.

In our previous study, the incorporation of Co–Zn ferrite into biochar primarily facilitated the solid–liquid separation; however, the enhancement of adsorption capacity was marginal.[25] In the present work, f-CNTs are introduced into the Co–Zn ferrite-incorporated biochar (CNT-CZB) to overcome this limitation by significantly enhancing the adsorption capacity. This study systematically evaluates the adsorption performance of the CNT-CZB nanocomposite in both synthetic aqueous solution and real tannery wastewater. The objectives of this study are to (i) synthesize and characterize the CNT-CZB nanocomposite, (ii) investigate the impact of CNTs and Co–Zn ferrite hybridization on the physical and chemical properties of biochar, (iii) examine the effect of solution pH, Cr concentration and reaction time on the adsorption capacity of the nanocomposite, (iv) explain the insights into the interaction mechanism of Cr ions adsorption with the CNT-CZB nanocomposite and (v) investigate the influence of three input variables (pH, concentration and reaction time) on Cr adsorption using BBD.

2. Experimental section

2.1. Materials

Water hyacinths (WH) are collected from a local pond in Chandpur, Bangladesh, as a biomass source. Multi-walled CNTs are sourced from CNano Technology Ltd, China. Iron(II) nitrate (≥98%), cobalt(II) nitrate (≥99%), zinc nitrate hexahydrate (≥99.5%), and potassium dichromate (≥99.9%) are purchased from Merck, Germany.

2.2. Preparation of WHB and CNT-CZB

WH stems are separated, washed with water, and dried for 48 h at 90 °C in an oven. The stems are milled into powder and pyrolyzed in a muffle furnace under oxygen-limited conditions for 2 h at 450 °C. After grinding, the biochar is sieved to obtain particles smaller than 250 μm. The synthesis of $Co_{0.5}Zn_{0.5}Fe_2O_4$ ferrites is reported in the previous study.[25] Briefly, an appropriate portion of metal nitrates is added to 100 mL of deionized (DI) water, and then NH_4OH is added gradually until its pH reaches 7.0. The solution is heated (5 °C min^{-1}) to 95 °C under continuous stirring for 1 h, forming a gel-like substance. At this temperature, the gel is converted into ash through auto-combustion. After washing and drying in an oven, the material is subjected to 6 h of annealing at 600 °C.

MWCNTs are functionalized using a mixture of concentrated nitric acid (HNO_3, 65%) and sulfuric acid (H_2SO_4, 98%) in a 1 : 3 volume ratio. The MWCNTs are sonicated in the acid mixture for 30 min using an ultrasonic probe sonicator (model 150 V T^{-1}), followed by refluxing at 80 °C for 4 h. Then, the mixture is washed multiple times with distilled water *via* centrifugation until a neutral pH is achieved. The f-CNTs are then dried in a vacuum oven at 60 °C for 72 h.

A suspension of 10 mg of f-CNTs in 100 mL of ethanol was sonicated using an ultrasonic probe sonicator for 30 min to achieve uniform dispersion. Then, 10 g biochar and 0.5 g Co–Zn ferrite are added to the suspension and continuously stirred for 1 h at 60 °C at a rate of 500 rpm. Finally, the CNT-CZB nanocomposite is washed with DI water and dried at 45 °C in an oven overnight. The synthesis process of the nanocomposite is shown in Fig. 1.

2.3. Adsorption experiments of synthetic water

A stock solution of Cr (1000 mg L^{-1}) is prepared by dissolving potassium dichromate in DI water. To investigate the adsorption of Cr, the stock solution is diluted to the expected concentration. In the batch experiments, 20 mg of adsorbent is mixed with 50 mL of Cr (100 mg L^{-1}) solution in a 100 mL glass beaker at 25 °C (±2 °C) temperature for 3 h. To adjust the pH of the Cr concentrated solution, HCl (0.1 M) and/or NaOH (0.1 M) are used. The effect of solution pH (2–10), reaction time (20–180 min), reaction temperature (30–60 °C), and initial Cr concentration (10–320 mg L^{-1}) on the Cr adsorption capacity is investigated. After filtration, the remaining residual is analyzed using atomic absorption spectroscopy to determine the total Cr concentration. The adsorption capacity (q_e) of Cr was derived from eqn (1).

$$q_e = \frac{C_i - C_e}{m} V \quad (1)$$

Where C_i and C_e are the initial and equilibrium concentration of Cr in mg L^{-1}, respectively. m (g) is the mass of the adsorbent and V (L) is the volume of the solution.

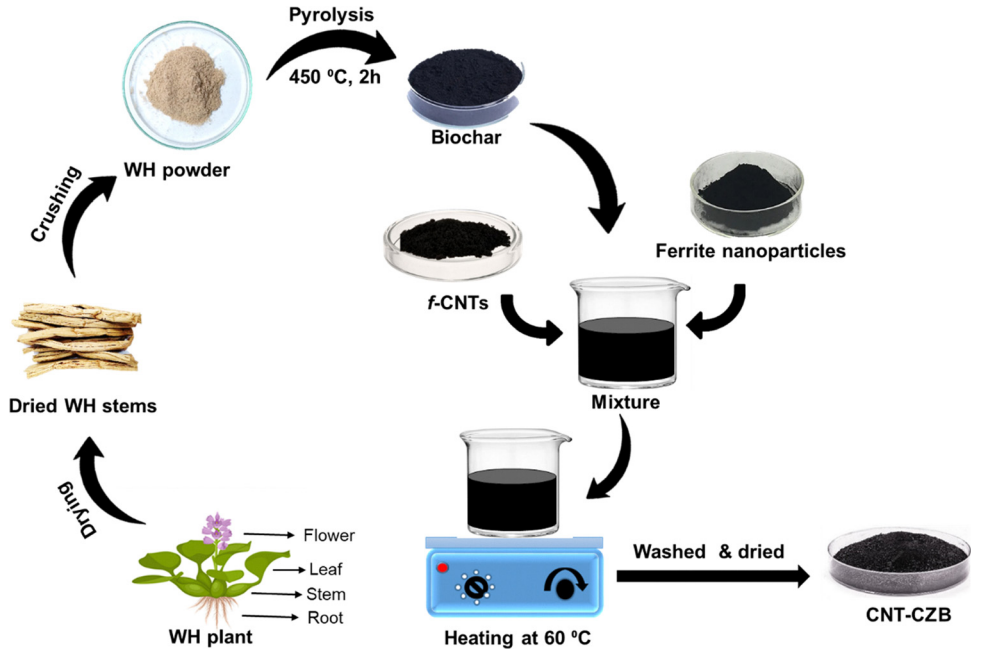

Fig. 1 Fabrication process of WHB modified with f-CNTs and Co–Zn ferrite.

The adsorption kinetics of Cr on the WHB and CNT-CZB nanocomposite are evaluated using the pseudo-first-order (PFO), pseudo-second-order (PSO), Elovich, and Weber–Morris kinetic models. The equations of the four models are as follows:

$$\text{PFO: } q_t = q_e(1 - e^{-k_1 t}) \quad (2)$$

$$\text{PSO: } q_t = \frac{k_2 q_e^2 t}{1 + k_2 q_e t} \quad (3)$$

$$\text{Elovich: } q_t = \frac{1}{\beta}\ln(1 + \alpha\beta t) \quad (4)$$

$$\text{Weber} - \text{Morris: } q_t = K_{id} t^{\frac{1}{2}} + C \quad (5)$$

The adsorption amount at time t is q_t (mg g^{-1}) and the equilibrium adsorbed amount is q_e (mg g^{-1}). k_1 (min^{-1}) and k_2 (g mg^{-1} min^{-1}) are the rate constants of PFO and PSO model, respectively. α and β are the initial adsorption rate (mg g^{-1} min^{-1}) and desorption constant (g mg^{-1}). K_{id} represents the intra-particle diffusion rate constant, and C is the intercept.

To analyze the adsorption isotherms of Cr, three models, namely the Langmuir, Freundlich, and Sips models, are used. The Langmuir model describes monolayer adsorption on a homogeneous surface with identical sites and is expressed in its nonlinear form in eqn (6).

$$q_e = \frac{q_m k_L C_e}{1 + k_L C_e} \quad (6)$$

The maximum adsorption capacity is q_m (mg g^{-1}), and K_L represents the Langmuir rate constant.

The Freundlich model explains adsorption as a multilayer process occurring on a surface with varying energy sites. Eqn (7) presents the Freundlich isotherm in its nonlinear form.

$$q_e = k_F C_e^{\frac{1}{n}} \quad (7)$$

Where K_F is a constant, and n reflects the strength of adsorption.

The Sips isotherm model combines features of the Langmuir and Freundlich isotherms with distinct adsorption sites. The non-linear form of this model is represented in eqn (8).

$$q_e = \frac{q_m (kC_e)^n}{1 + (kC_e)^n} \quad (8)$$

Where k (L mg^{-1}) and n are the Sips equilibrium constant and Sips model exponent, respectively.

Thermodynamic parameters, including the Gibbs free energy change (ΔG°), enthalpy change (ΔH°), and entropy change (ΔS°), are evaluated to understand the spontaneity, nature, and disorder associated with the adsorption process. These parameters are determined using the following equations.

$$\ln K_d = \frac{\Delta S^\circ}{R} - \frac{\Delta H^\circ}{RT} \quad (9)$$

$$\Delta G^\circ = \Delta H^\circ - T\Delta S^\circ \quad (10)$$

Where K_d $\left(K_d = \frac{q_e}{C_e}\right)$ is known as the distribution coefficient, R is the universal gas constant, and T is the absolute temperature of the solution, respectively. The intercept and slope of the $\ln K_d$ *versus* $1/T$ provide the values of ΔS° and ΔH°, respectively.

2.4. Adsorption experiments of tannery wastewater

The adsorption experiment with real tannery wastewater is conducted at the native pH (3.54 ± 0.12) without dilution to

evaluate the adsorption performance under realistic effluent conditions.

2.5. Box–Behnken design (BBD)

The Design-Expert 10.0 software is used to design the experiment and fit quadratic models to understand the relationship between input variables and response. Solution pH (X_1: 2–10), Cr concentration (X_2: 10–320 mg L^{-1}), and reaction time (X_3: 20–180 min) are the three variables, and adsorption capacity (q_e) is the response. To investigate the interactive effects of selected parameters, 17 experimental runs are designed using the BBD. The following second-order polynomial equation was used to express the response variable.

$$Y = \beta_0 + \sum \beta_i X_i + \sum \beta_{ii} X_i^2 + \sum \beta_{ij} X_i X_j + \varepsilon \qquad (11)$$

Where Y is the response, β_0 and β_i are the intercept and the linear coefficients, respectively. β_{ii} and β_{ij} are the quadratic coefficients and the interaction coefficients, respectively. The variables X_i and X_j are independent, and ε represents the error term.

2.6. Characterization

The detailed characterization data are provided in the SI.

3. Results and discussion

3.1. Surface morphology

The FESEM and TEM images of pristine WHB, MWCNTs, and the CNT-CZB nanocomposite are shows in Fig. 2. The FESEM and TEM images of pristine WHB (Fig. 2(a) and (b)) reveal a rough, uneven, and irregular surface texture, a characteristic feature of biochar derived from lingo-cellulosic biomass. WHB biochar exhibits irregular cracks with moderate porosity, likely developed during the release of volatiles during pyrolysis. TEM analysis confirms the structural features of CNTs, revealing a multi-walled, tubular morphology with an average inner diameter of approximately 13 nm and a wall thickness of 5 nm (Fig. 2c). The interlayer spacing (*d*-spacing) of the CNTs is measured to be 0.341 nm, corresponding to the (002) crystallographic plane, confirming their graphitic nature (Fig. 2d). The CNT-CZB nanocomposite displays a dense network of randomly oriented CNTs distributed across the surface, as observed in FESEM and TEM images (Fig. 2(e) and (f)). Furthermore, small bright regions visible in the nanocomposite's FESEM image (Fig. 2e) indicate the uniform distribution of Co–Zn ferrite nanoparticles in the biochar matrix. These modifications introduce surface irregularities, enhance pore development, and increase the number of active sites available for adsorption. These findings demonstrate the successful integration of CNTs and Co–Zn ferrite nanoparticles into the biochar matrix. Additionally, the EDX spectra of the CNT-CZB nanocomposite before and after Cr adsorption (Fig. 2(g) and (h)) reveal a distinct Cr peak in the nanocomposite's spectrum after adsorption. In contrast, no such peak is observed before adsorption. This result confirms effective Cr adsorption onto the CNT-CZB nanocomposite, highlighting its potential as an efficient adsorbent for Cr removal.

Fig. 3(a) and (b) represents the surface roughness analysis of raw WHB and CNT-CZB nanocomposite using FESEM images processed with ImageJ software. The 3D surface plot of the CNT-CZB nanocomposite shows a rougher, more uneven texture than the WHB. The roughness, characterized by cracks and pores on the WHB surface, results from the carbonization process. When dispersed onto the biochar surface, the tubular and fibrous nature of CNTs enables them to adhere to the surface and form a 3D porous network, thereby enhancing surface area and roughness. The increase in surface roughness is a key factor in improving the adsorption performance of CNT-CZB nanocomposite.

3.2. BET analysis

The specific surface area and pore characteristics of the WHB and the nanocomposite are investigated using the BET method. The adsorption–desorption isotherms for both adsorbents exhibited a type IV pattern as shown in Fig. 4(a) and (b). The results reveal an increase of surface area from 35.64 to 75.94 m^2 g^{-1}, a slight rise in total pore volume from 0.104 to 0.122 cm^3 g^{-1}, and a reduction of average pore diameter from 35.15 to 20.4 nm (Fig. 4(c) and (d)) due to the incorporation of CNTs and ferrite nanoparticles. These findings align closely with FESEM observations, which show a transformation from relatively large pores in WHB to a denser and more organized mesoporous structure (2–50 nm) in the nanocomposite.

Although the average pore diameter is decreased to 20.4 nm after the incorporation of CNTs and Co–Zn ferrite, the pores remain within the mesoporous range, which is sufficient for Cr ion diffusion. Moreover, the higher surface area and improved pore network enhance the accessibility of active adsorption sites.

3.3. Structural and compositional analysis

XRD analysis of WHB and the CNT-CZB nanocomposite is shown in Fig. 5(a). The XRD analysis indicates the amorphous structure of WHB. The peaks at 28.5° (200) and 40.6° (220) are due to the presence of KCl.[26] The peak at 29.5° (104) was likely due to the $CaCO_3$. The WHB contained a small amount of quartz, indicated by the peaks at 50.2° (112) and 58.6° (211).[27] The presence of KCl, $CaCO_3$ and quartz in the WHB indicates the absorption of minerals from the water source. The Co–Zn ferrite and CNT-incorporated biochar nanocomposite shows distinct peaks at 24.0° (002), 30.0° (220), 35.46° (311), 43.1° (400), 56.96° (511), and 62.54° (440).[28] The peak at ~24.0° in the CNT-CZB nanocomposite is attributed to the graphitic structure (sp^2 hybridized carbon layers), and the other peaks confirmed the cubic spinel structure of Co–Zn ferrite.[29]

Fig. 5(b) represents the FT-IR spectra of the nanocomposite before and after Cr adsorption from an aqueous solution. The functionalization of CNTs in the CNT-CZB nanocomposite introduced oxygen-containing functional groups, as evidenced by the C=O stretching vibrations at 1714 cm^{-1} and O–H

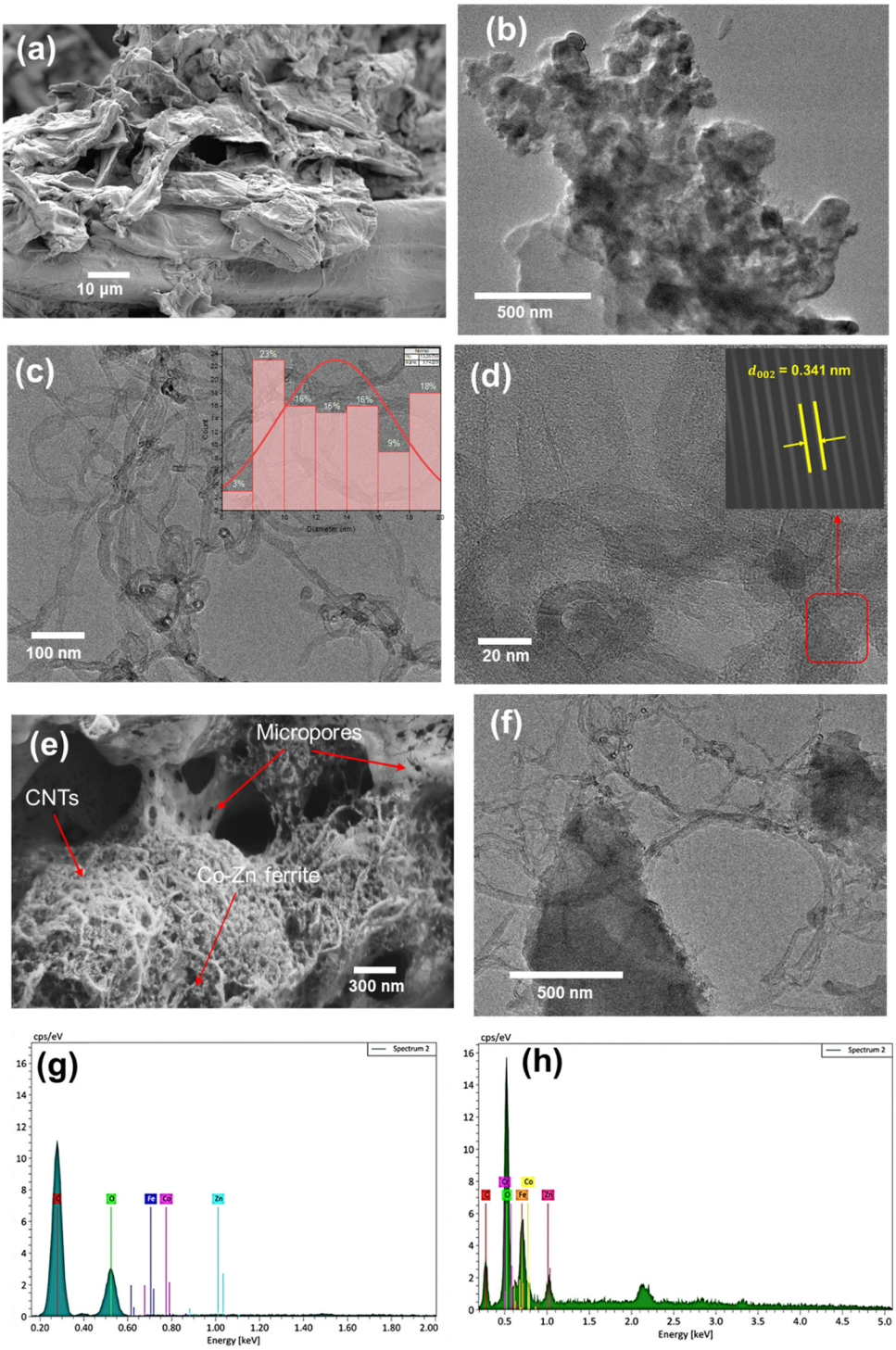

Fig. 2 (a) and (b) FESEM and TEM images of WHB, (c) TEM images of MWCNTs (inset: diameter distribution curve of MWCNTs, (d) HRTEM image of MWCNTs (inset: *d*-spacing of MWCNTs), (e) and (f) FESEM and TEM images of CNT-CZB nanocomposite, and (g) and (h) EDX of CNT-CZB nanocomposite before and after Cr adsorption.

stretching vibrations in the range of 2400–3600 cm^{-1}.[30–32] The peak of around 1100 cm^{-1} is associated with the S═O stretching vibrations of the sulfonate group, which results from CNT functionalization using H_2SO_4.[33] A weak peak near 1600 cm^{-1} is attributed to the graphitic sp^2 hybridized C═C bonds, characteristic of CNTs.[32] The 590 cm^{-1} peaks correspond to Fe–O stretching vibrations, confirming the presence of ferrite structures.[34] The decrease in the intensity of the C═O peak following Cr adsorption suggests that these functional groups may be involved in complexation with Cr ions. The shift of the

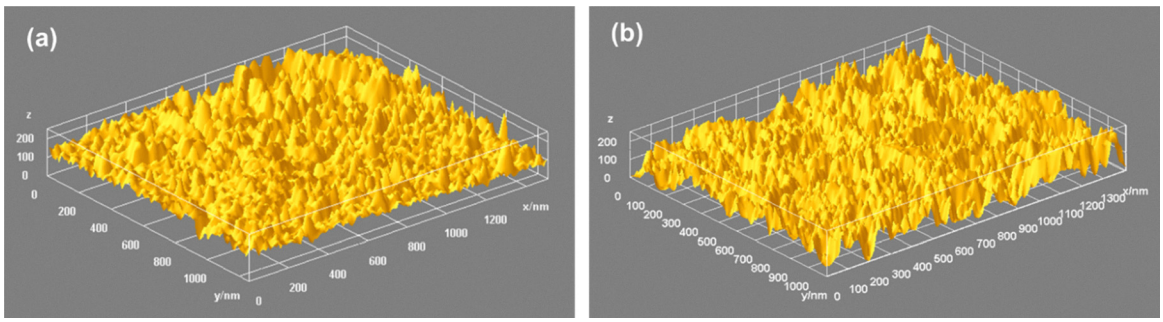

Fig. 3 The 3D surface plot of (a) WHB and (b) CNT-CZB nanocomposite.

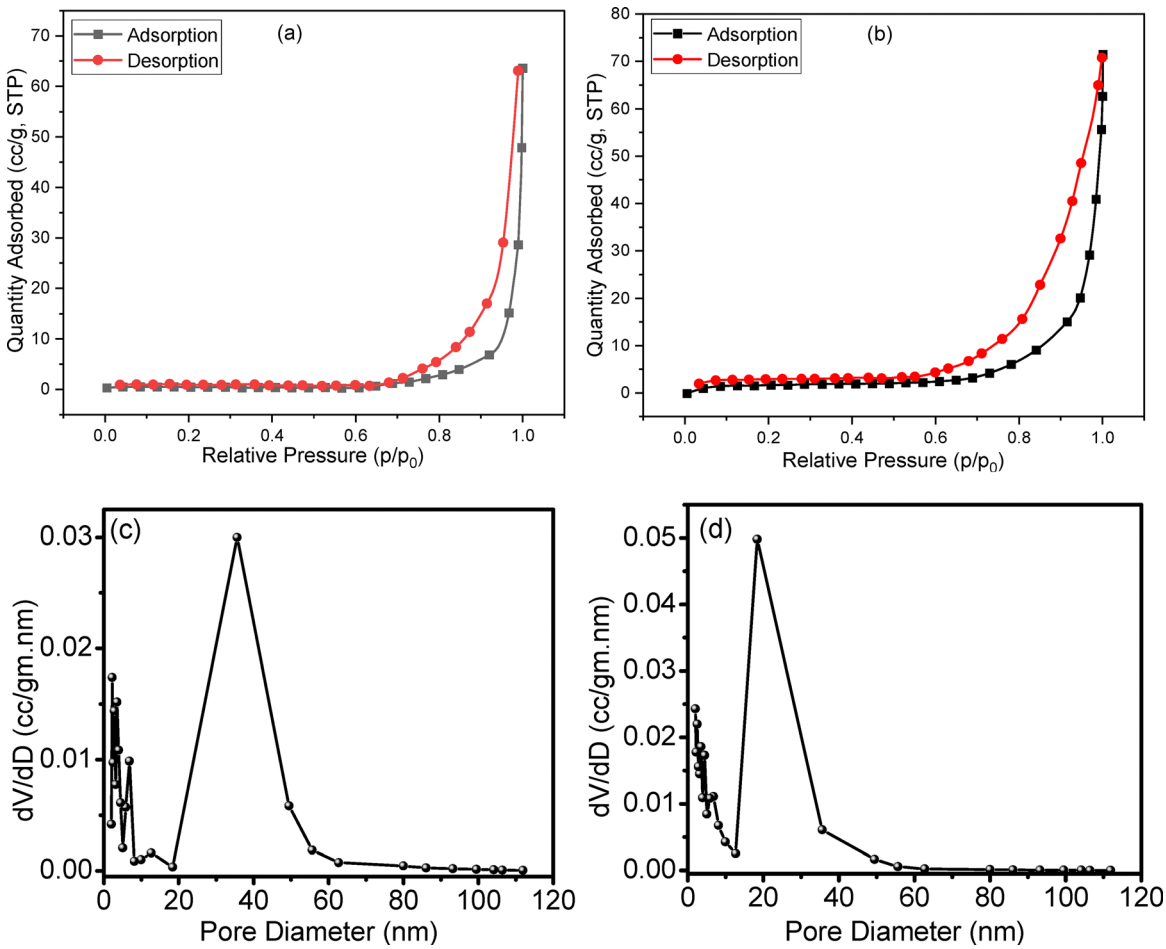

Fig. 4 (a) and (b) Adsorption isotherms and (c) and (d) pore-size distribution of WHB and CNT-CZB nanocomposite using N_2 gas adsorption.

S═O peak to a higher wavenumber indicates that Cr ions interact with the functional groups alters the bond strength and electron distribution. Two new peaks appear near 950 cm^{-1} and 754 cm^{-1} in the nanocomposite after Cr ions adsorption. These peaks are attributed to Cr–O and Cr–O–Cr stretching vibrations, respectively, confirming successful adsorption of Cr ions onto the nanocomposites.[35] The FT-IR analysis demonstrated that the adsorption mechanism involved chemical interactions between Cr ions and the functional groups (C═O and S═O) on the nanocomposite surface.

3.4. Chemical state analysis

XPS analysis is carried out to investigate the oxidation states of elements in the nanocomposite, as shown in Fig. 6. A strong peak of Cr 2p is observed after adsorption, which confirms the successful adsorption of Cr on the nanocomposite (Fig. 6a). Cr has two peaks of $2p_{3/2}$ and $2p_{1/2}$ orbitals, as shown in Fig. 6(b). The peaks at 577.02 and 587.09 eV correspond to Cr(III), whereas the peaks at 578.75 and 589.08 eV are associated with Cr(VI).[36] After adsorption, the presence of both Cr(VI) (38.2%) and Cr(III) (61.8%) on the nanocomposite surface suggested

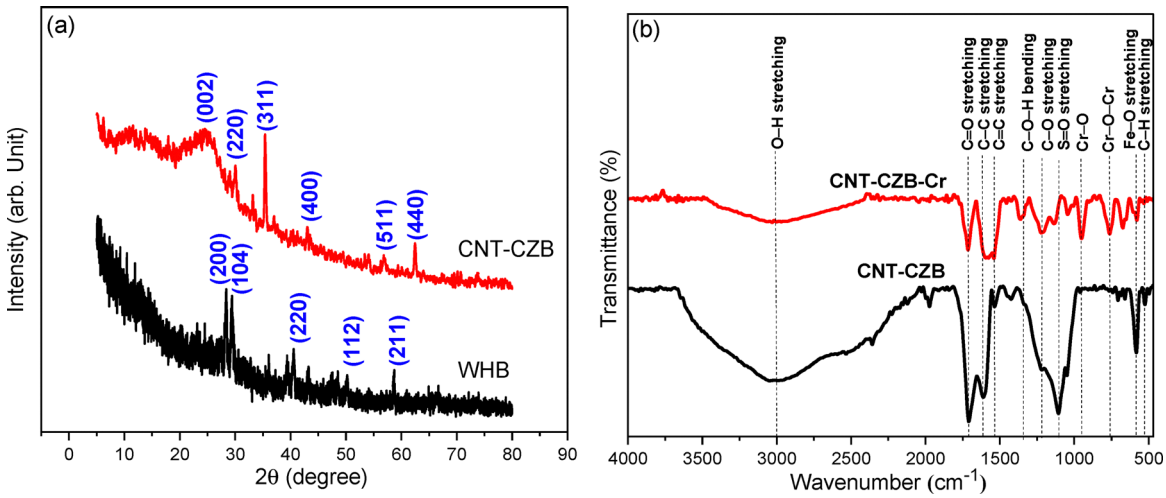

Fig. 5 (a) XRD pattern of WHB and CNT-CZB nanocomposite, (b) FT-IR spectra of CNT-CZB nanocomposite before and after Cr adsorption.

that Cr(VI) is converted to Cr(III). A decrease in C–O (from 29.3% to 17.2%) and C═O (from 5.9% to 3.85%), as shown in Fig. 5c, indicates that Cr(VI) adsorption involves electron transfer from these functional groups present on biochar and CNTs, which facilitated the reduction of Cr(VI) to Cr(III). The increase in the C–C bond suggested a decrease in oxygen-containing functional groups due to redox reactions, which formed Cr(III) species on the surface and Cr(III) interaction with these sites. A significant reduction in –OH groups (from 43.16% to 26.3%) further supports the reduction of Cr(VI) to Cr(III) *via* surface interactions and the participation of this group as active Cr adsorption sites.

3.5. Raman spectroscopic analysis

Fig. S1 represents the Raman spectra of CNT-CZB nanocomposite collected with an excitation of 514 nm. The band observed at 1604 cm^{-1} corresponds to the G band arising from the in-plane stretching vibration of sp^2-bonded carbon atoms, confirming the presence of graphitic domains from CNTs.[37] The band near 1330 cm^{-1} is assigned to the D band, which originates from defect-induced vibrations of sp^2 carbon rings.[38] An additional band around 1450 cm^{-1} is observed, which is attributed to amorphous carbon species randomly distributed within the graphitic framework. Furthermore, a prominent band is observed near 630 cm^{-1}, related to the A_{1g} symmetric stretching vibration of Fe–O bonds in the spinel Co–Zn ferrite structure, confirming the successful incorporation of the ferrite with CNT–biochar matrix.[39]

3.6. Magnetic properties

The magnetic behavior of the Co–Zn ferrite and CNT-CZB nanocomposite is examined at 300 K over a magnetic field range of −20 000 to 20 000 Oe, as shown in Fig. S2. A narrow hysteresis loop is observed in the ferrite nanoparticles along with a saturation magnetization of approximately 53 emu g^{-1}, whereas the nanocomposite exhibits a saturation magnetization of 3 emu g^{-1}. The magnetization of the nanocomposite is low due to the incorporation of non-magnetic CNTs and biochar into the ferrite structure. Despite the low magnetization, the composite retains sufficient magnetic properties to allow efficient separation from the liquid medium following the adsorption.

3.7. Effect of solution pH

The pH of the solution significantly influenced the adsorption capacity of Cr onto the CNT-CZB nanocomposite. The highest adsorption capacity (78.93 mg g^{-1}) is observed at pH 2, whereas the lowest (58.26 mg g^{-1}) occurred at pH 10 (Fig. 7a). Under acidic conditions, the nanocomposite surface becomes highly protonated due to the high concentration of H^+ ions in the solution. As a result, the adsorbent surface develops a positive charge, which enhances electrostatic attraction between the nanocomposite and the negatively charged Cr(VI) species, present as $HCrO_4^-$ and $Cr_2O_7^{2-}$ in acidic media. The electrostatic interaction between these species and the positively charged surface facilitates adsorption. As the pH increases, the concentration of OH^- ions in the solution rises, resulting in the deprotonation of the nanocomposite surface. This results in a negatively charged surface, which creates electrostatic repulsion between the adsorbent and the negatively charged Cr(VI) species, primarily existing as CrO_4^{2-} under alkaline conditions. This repulsion weakens the adsorption process, resulting in a lower adsorption capacity. The protonation and deprotonation reaction can be expressed as:

$$\text{CNT-CZB–OH} + H^+ \rightarrow \text{CNT-CZB–OH}_2^+.$$

$$\text{CNT-CZB–OH} + OH^- \rightarrow \text{CNT-CZB–O}^- + H_2O.$$

The point of zero charge (pH_{PZC}) of the CNT-CZB absorbent is determined using the pH drift method. The point at

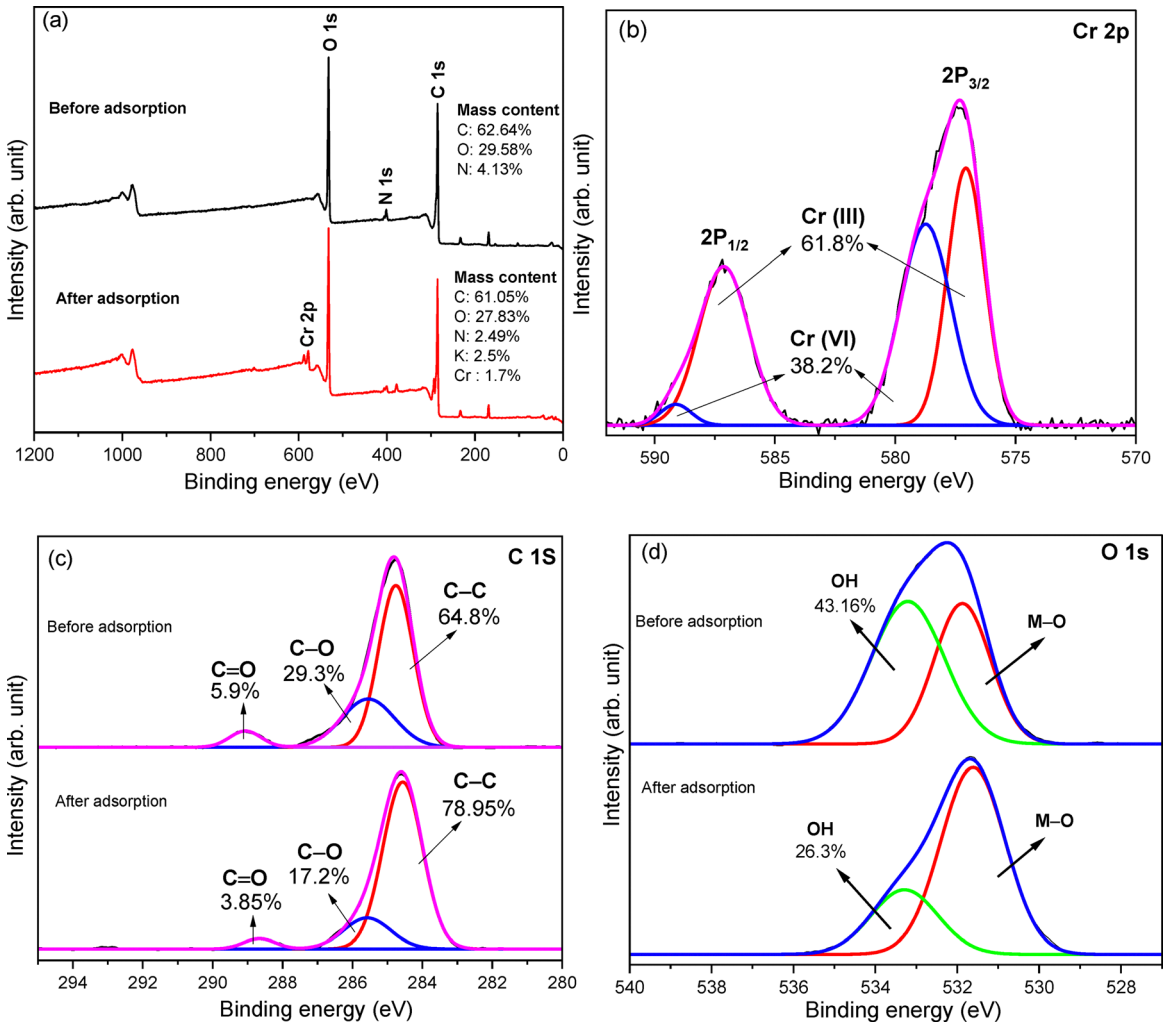

Fig. 6 (a) XPS survey spectra of CNT-CZB. Narrow spectra of (b) Cr 2p, (c) C 1s, and (d) O 1s before and after adsorption.

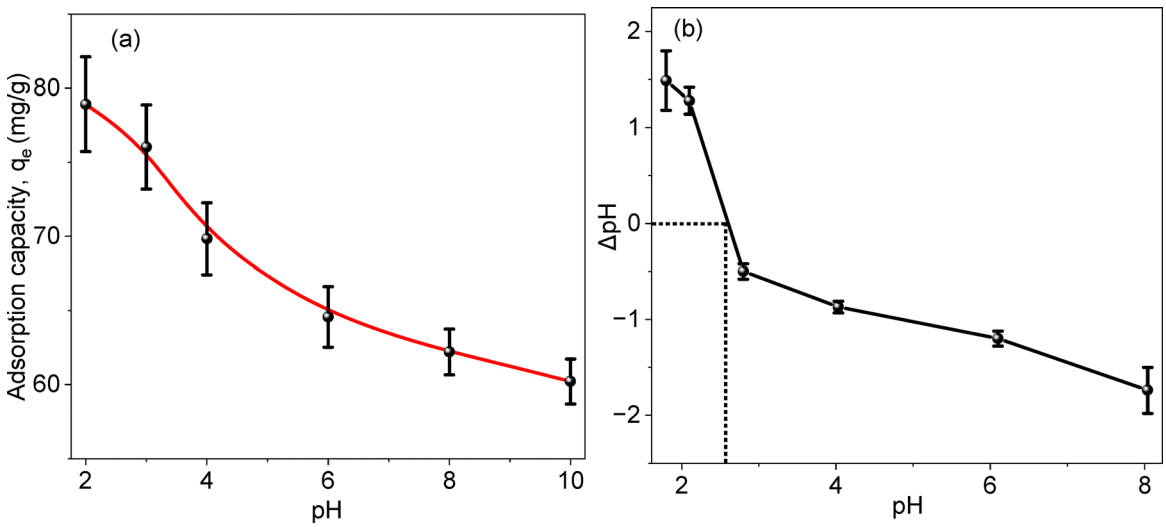

Fig. 7 (a) Effect of solution pH on the Cr adsorption capacity and (b) determination of the point of zero-charge (pH_{PZC}) of the CNT-CZB nanocomposite.

which ΔpH equals zero is observed at approximately pH 2.6, indicating the pH_{PZC} of the adsorbent (Fig. 7b). Below this pH, the adsorbent surface becomes positively charged due to protonation.

3.8. Adsorption kinetics

As shown in Fig. 8(a) and (b), the Cr adsorption rate is fast in the initial stage, then gradually slows down, and finally reaches equilibrium at around 120 min for WHB and 60 min for CNT-CZB adsorbents. The CNT-CZB demonstrated an adsorption capacity of ~81 mg g^{-1}, whereas it is ~48 mg g^{-1} for WHB, indicating that CNTs serve as active sites for Cr ions. Table S1 shows that the PSO model provided an excellent fit for both adsorbents. For CNT-CZB the PSO model shows a higher correlation coefficient (R^2 = 0.995 and adj. R^2 = 0.994) and lower error parameters (χ^2 = 0.939 and RSS = 3.75) than the PFO and Elovich models. Moreover, the maximum adsorption capacity calculated from the PSO model (80.62 ± 0.563) is in close agreement with the experimentally observed value (78.12 ± 1.58), further confirming the suitability for describing the adsorption kinetics. It indicates that the adsorption is primarily chemically controlled, with the equilibrium adsorption capacity closely matching experimental values for the CNT-CZB adsorbent. During adsorption, Cr(VI) species are partially reduced to Cr(III) (Fig. 6b). Carboxyl groups on the adsorbent surface form inner-sphere complexation with Cr(III), while –OH groups contribute through hydrogen bonding interactions. These oxygen-containing functional groups play a crucial role in the efficient removal of Cr from wastewater.[40]

The Elovich model further supported the chemisorption hypothesis, highlighting the heterogeneous surface of the nanocomposite with a high initial adsorption rate (α = 7.85 mg g^{-1} min^{-1}) and a moderate desorption (β = 0.118 g mg^{-1}). The rapid initial adsorption can be attributed to the increased surface area, slight rise in pore volume, and interconnected mesoporous network resulting from the incorporation of CNTs and Co–Zn ferrite nanoparticles.

The Weber–Morris model, as shown in Fig. 8(c), revealed a three-stage process: rapid initial film diffusion ($K_{id,1}$ = 7.105 ± 0.86 mg g^{-1} $min^{-0.5}$), gradual intra-particle diffusion

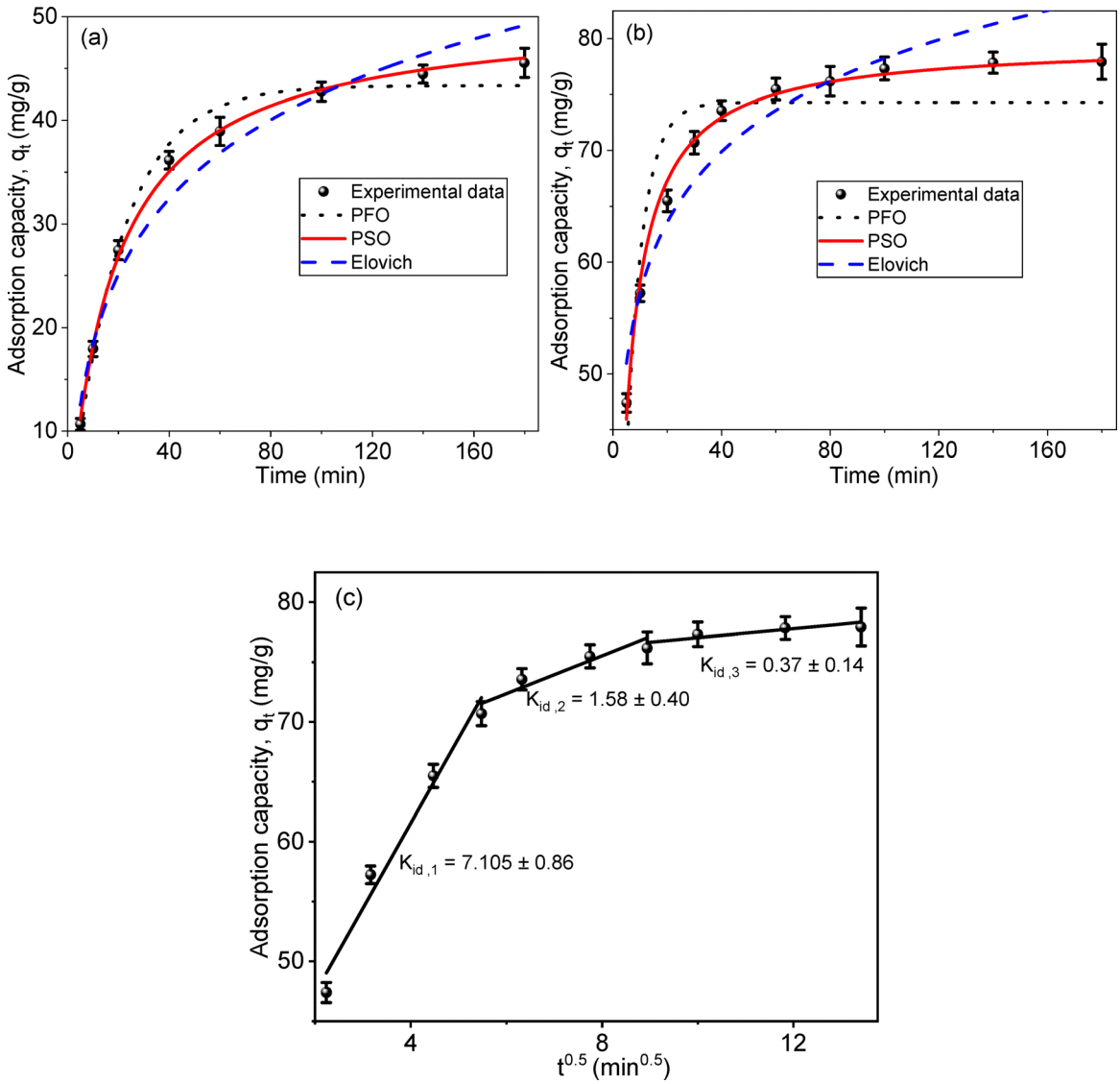

Fig. 8 Adsorption kinetics of Cr on (a) WHB, (b) CNT-CZB nanocomposite, and (c) intra-particle diffusion model of Cr on the CNT-CZB nanocomposite.

($K_{id,2}$ = 1.58 ± 0.40 mg g^{-1} $min^{-0.5}$), and final equilibrium ($K_{id,3}$ = 0.37 ± 0.14 mg g^{-1} $min^{-0.5}$). The multilinear behavior with a non-zero intercept indicates that intra-particle diffusion contributes to adsorption, but it is not the sole rate-limiting step.[41] Overall, the PSO model best describes the kinetics, confirming chemisorption as the dominant mechanism, while the Elovich and Weber–Morris models highlighting the heterogeneous surface and multi-stage nature of the adsorption process.

3.9. Adsorption isotherms

Adsorption isotherms provide valuable insights into the adsorption mechanisms of Cr onto the adsorbent. Fig. 9 shows the fitting of various adsorption isotherm models to the experimental data of the WHB and CNT-CZB nanocomposite. For WHB, the Langmuir isotherm exhibited the highest coefficient of determination (R^2 = 0.980) and the adj. R^2 (0.969), along with the lowest χ^2 (1.58) and RSS (7.93), indicating it is the best-fitting model for the experimental data. Additionally, the Sips exponent (n) value was close to 1, indicating Langmuir-type behavior. It suggested that Cr adsorption on the WHB involved monolayer adsorption.[42]

Table S2 shows that the Sips isotherm exhibits the best overall fit to the experimental data, as evidenced by the highest R^2 (0.988) and the adj. R^2 (0.985), along with the lowest χ^2 (15.12) and RSS (2.52) among all tested models for the CNT-CZB adsorbent. The value of q_m (78.33 mg g^{-1}) predicted by the Sips model is in close agreement with the experimentally observed value (79.80 mg g^{-1}), indicating this model best describes the adsorption process.

The Sips model suggests that the adsorption process involves mixed mechanisms of Langmuir and Freundlich isotherms. The heterogeneity factor ($1/n$) in this case is 0.79, indicating that both monolayer and multilayer adsorption occur on a heterogeneous surface.[43] This dual behavior aligns with the complex structural and compositional nature of the CNT-CZB nanocomposite. Generally, biochar has relatively uniform adsorption sites in terms of surface functional groups and pore characteristics, resulting in monolayer adsorption. However, the incorporation of CNTs and ferrite nanoparticles introduces significant surface heterogeneity, resulting in adsorption sites with varied binding energies, as confirmed by surface morphology analysis. Additional functional groups and defects in CNTs create a broader distribution of adsorption site energies and facilitate the coexistence of strong and weak binding sites. As a result, a mixed monolayer and multilayer adsorption of Cr ions occur on the CNT-CZB nanocomposite surface.[27]

3.10. Thermodynamic parameters

Thermodynamic parameters of Cr adsorption by the CNT-CZB nanocomposite are calculated from Fig. S3 and presented in Table 1. The negative ΔG° values for the adsorption process confirm that the process is spontaneous and thermodynamically favorable. The enthalpy change (ΔH°) is around 49 kJ mol^{-1}, a positive value, indicating that the adsorption process is endothermic. This suggests that the adsorption capacity increases with temperature. The magnitude of ΔH° is greater than 40 kJ mol^{-1}, suggesting a chemisorption nature of the adsorption process. Furthermore, the entropy change (ΔS°) is calculated to be 0.176 kJ mol^{-1} K^{-1}, indicating an increase in randomness or disorder at the solid–liquid interface during adsorption. The positive ΔS° value suggests that the adsorption process involves a significant rearrangement of the adsorbent–adsorbate system, likely due to the nanocomposite material's surface properties and functional groups.

3.11. Adsorption mechanism

The experimental findings of this work reveal that incorporating CNTs into the biochar matrix significantly enhanced the Cr adsorption capacity. In the EDX spectra as shown in Fig. 2(h), a distinct Cr peak appears in the nanocomposite's spectrum after adsorption. The presence of two Cr–O and Cr–O–Cr peaks near 950 cm^{-1} and 754 cm^{-1} in the FT-IR spectrum after adsorption

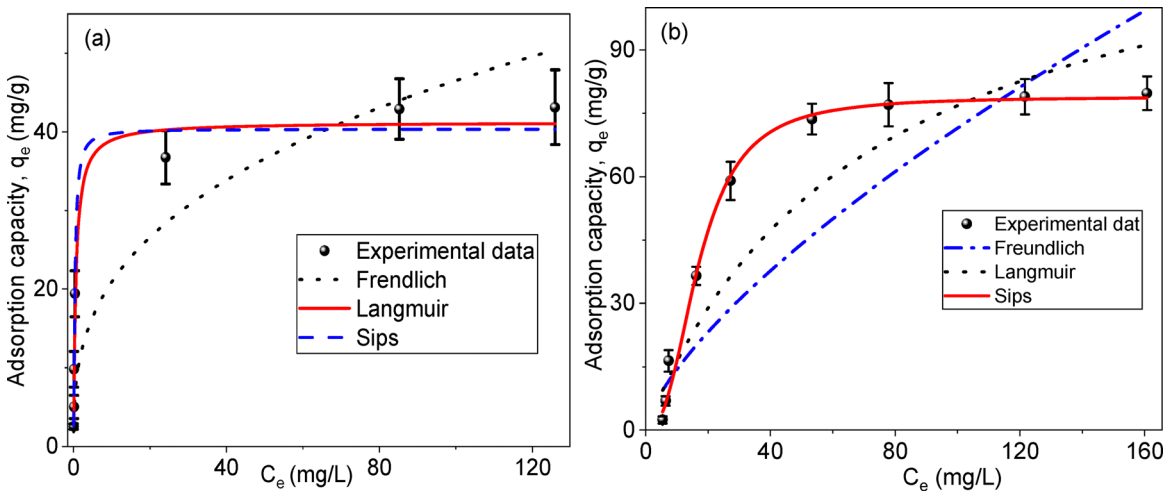

Fig. 9 Langmuir, Freundlich, and Sips isotherm models for Cr(VI) adsorption on (a) WHB and (b) CNT-CZB nanocomposite.

Table 1 Thermodynamic analysis of Cr adsorption on the CNT-CZB nanocomposite

Parameters	Values (303 K)	(313 K)	(323 K)	(333 K)
ΔG° (kJ mol^{-1})	−3.85	−5.38	−7.15	−8.90
ΔH° (kJ mol^{-1})	49.7 ± 1.01			
ΔS° (kJ mol^{-1} K^{-1})	0.176 ± 0.032			

indicates the effective adsorption of Cr ions onto the CNT-CZB nanocomposite (Fig. 5b). In the XPS spectra as shown in Fig. 6b, the presence of both Cr(VI) (38.2%) and Cr(III) (61.8%) on the nanocomposite surface after adsorption suggest that Cr(VI) is partially converted to Cr(III). This reduction process is more prominent in acidic conditions (pH ≤ 4.0).

$$HCrO_4^- + 7H^+ + 3e^- \rightarrow Cr^{3+} + 4H_2O$$

$$Cr_2O_7^{2-} + 14H^+ + 6e^- \rightarrow 2Cr^{3+} + 7H_2O$$

Fig. 6(c) shows that the relative area of C–O decreased from 29.3% to 17.2% and that of C═O decreased from 5.9% to 3.85%. This finding suggested that those oxygen-containing functional groups contributed to the reduction of Cr(VI) to Cr(III) by donating electrons.[36] After adsorption, the increase in the C–C bond (64.8 to 78.95%) revealed a decrease in oxygen-containing functional groups. A significant reduction in –OH groups from 43.16% to 26.3% (Fig. 6d) further supported that oxygen-containing functional groups act as active Cr adsorption sites.[13] In the FT-IR spectra as shown in Fig. 5(b), a decrease in the intensity of the C═O and S═O peaks following Cr adsorption suggested that these functional groups may be involved in complexation with Cr(III) ions. BET analysis (Fig. 4) reveals an increase in surface area resulting from the incorporation of CNTs into the composite. The increased surface area provides more active sites for Cr ions. The adsorption capacity increased from 44.58 to 78.12 mg g^{-1}, and the adsorption per unit surface area (site density) decreased slightly (1.25 to 1.03 mg m^{-2}). This finding suggests that the enhanced performance is not solely due to surface area expansion. Instead, the introduction of CNTs and ferrite may provide additional active sites, thereby enhancing the overall adsorption behavior.

The possible mechanism of Cr adsorption on the CNT-CZB nanocomposite involves physicochemical processes. Initially, Cr(VI) is electrostatically attracted to protonated surface sites, while a fraction of the Cr ions becomes trapped within the pores of the adsorbent. During adsorption, a portion of Cr(VI) is converted to Cr(III) by electron-donating functional groups. The resulting Cr(III) forms inner-sphere complexation with oxygen-containing functional groups.

3.12. Effect of co-existing ions on the adsorption capacity of Cr

To examine the practical applicability of CNT-CZB nanocomposite, the effect of co-existing ions on Cr adsorption is investigated (Fig. S4). A negligible change in Cr adsorption capacity is observed in the presence of Na^+ and Cl^- as co-existing ions. Na^+ is a monovalent cation with low charge density and does not significantly compete with Cr(III) for adsorption sites. At the same time, Cl^- does not form stable complexes with Cr(VI) or Cr(III). In contrast, divalent and multivalent ions (Ca^{2+}, Fe^{3+}, and SO_4^{2-}) significantly reduced the adsorption capacity. Generally, Cr(III) binds strongly with oxygen-containing functional groups. When Ca^{2+} or Fe^{3+} ions occupy these oxygen sites, Cr(III) complexation is also reduced. The presence of SO_4^{2-} ions increase the ionic strength of the solution, which reduces the surface potential. As a result, the electrostatic attraction between surface sites and Cr(VI) anions becomes weaker, further reducing adsorption.

3.13. Reusability performance

To evaluate the practical reusability of the CNT-CZB adsorbent, a recycling test is conducted as shown in Fig. S5. Experimental results revealed a ∼10% reduction in adsorption capacity by the 3rd cycle and nearly 50% by the 5th cycle. The oxygen-containing functional groups (–OH, –COOH, *etc.*) present in the adsorbent play a crucial role in adsorption. A partial reduction from Cr(VI) to Cr(III) occurs during the adsorption process. The reduced Cr(III) species exhibit a stronger affinity for the adsorbent surface due to its tendency to form stable complexes with oxygen donor groups. Although this complexation significantly enhances the adsorption capacity, it also hinders the complete desorption of Cr during regeneration. As a result, a gradual decrease in adsorption capacity is observed during repeated recycling tests.

3.14. Application to the tannery wastewater

Leather tanning processes utilize Cr salts, such as chromium sulfate, to create chemical cross-links between collagen chains, which stabilize the fiber network. Chrome tanning wastewater contains a high concentration of Cr in dissolved and precipitated forms. In this study, tannery wastewater is collected from the Sarwar Leather Complex Ltd, Bangladesh Small and Cottage Industries Corporation (BSCIC), Tannery Industrial Estate, Savar, Dhaka. Table 2 represents the elemental analysis of the tannery wastewater, which revealed a high concentration of Cr(III) (3867 ± 14 mg L^{-1}) along with Na (38 ± 3 mg L^{-1}), Ca (120 ± 5 mg L^{-1}), Cl^- (1757 ± 35 mg L^{-1}), and SO_4^{2-} (21 000 ± 165 mg L^{-1}), while Fe is below the detection limit. The UV-vis spectra (Fig. S6) show a clear difference between the synthetic sample and the tannery wastewater sample. The synthetic

Table 2 Comparison of solution parameters before and after treatment of tannery wastewater

Concentration	Tannery wastewater	After adsorption using CNT-CZB	Unit
Cr(III)	3867 ± 14	2480 ± 11	mg L^{-1}
Na	38 ± 3	24 ± 2	mg L^{-1}
Ca	120 ± 6	48 ± 3	mg L^{-1}
Fe	—	—	mg L^{-1}
SO_4^{2-}	21 000 ± 165	16 000 ± 120	mg L^{-1}
Cl^-	1757 ± 35	179 ± 16	mg L^{-1}

Table 3 Comparison of the adsorption capacity of Cr from contaminated water using different adsorbents

Adsorbent	Source of biomass	Pollutant	Concentration (mg L^{-1})	pH	Reaction time (min)	Adsorbent capacity (mg g^{-1})	Ref.
Biochar–Fe_3O_4	*Acacia falcata* leaf	Cr(VI)	25	2	120	36.15	47
PVA-AMC-HB) composite		Cr(III)	200	5	20	24.75	12
L-Cysteine-modified chitosan with polyacrylamide	—	Cr(VI)	300	3	—	18.98	48
Chitosan/kaolinite nanocomposite	Shrimp shells	Cr(VI)	270	4	120	173.8	49
Biochar–Co–Zn ferrite	Water hyacinth	Cr(VI)	320	2	180	52.15	25
		Cr(III)	3867	3.54	120	66.38	
Biochar–Co–Zn ferrite–CNTs	Water hyacinth	Cr(VI)	320	2	120	81	This
		Cr(III)	3867	3.54	120	101	study

sample (potassium dichromate solution) exhibits strong peaks at ~257.5 and 351 nm, consistent with the presence of chromate or dichromate.[44] In contrast, the tannery sample shows absorption peaks at ~420 and ~580 nm, consistent with Cr(III) complexation.[45] In tannery effluents, Cr exists in the trivalent form [Cr(III)], due to widespread use of chromium sulfate as the tanning agent, and at low pH, Cr(III) is mostly present as $[Cr(H_2O)_6]^{3+}$.

An adsorption capacity of ~101 mg g^{-1} is achieved using CNT-CZB as an adsorbent at a contact time of 2 h at 298 K for tannery wastewater. Cr(III) has a strong tendency to form stable complexes (inner-sphere coordination bond) with oxygen donor functional groups (–COOH, –OH, *etc.*) on the adsorbent surface.[46] These complexes are stronger and more stable than the outer sphere electrostatic interaction involved in Cr(VI) adsorption. As a result, the Cr adsorption capacity of the CNT-CZB nanocomposite is slightly higher for tannery wastewater than for the low-concentration synthetic water. A comparison of Cr adsorption capacities of various adsorbents for contaminated water is shown in Table 3.

3.15. Statistical analysis of Cr adsorption by Box–Behnken design

The Box–Behnken design (BBD) is used to optimize the Cr adsorption process, examining the impact of three independent variables: solution pH (X_1), initial concentration of Cr (X_2), and reaction time (X_3). Each variable is studied at three levels (low (−1), center (0), and high (1)), and the adsorption capacity (q_e) is chosen as the response. The designed experiments consisted of 17 runs, and the results are presented in Table S3. The regression analysis results established a quadratic polynomial model (eqn (12)) to predict the Cr(VI) adsorption capacity.

$$q_e = 38.3 - 8.19X_1 + 23.33X_2 + 6.86X_3 - 5.03X_1X_2 - 3.85X_1X_3 - 1.14X_2X_3 + 3.53{X_1}^2 - 5.25{X_2}^2 - 1.19{X_3}^2 \quad (12)$$

Fig. S7 represents the predicted *versus* actual plot, demonstrating a strong agreement between the experimental and model-predicted values of Cr adsorption capacity. The quadratic model developed using BBD is statistically significant, as indicated by the analysis of variance (ANOVA). Conventionally, a p-value less than 0.05 is considered statistically significant. As shown in Table S4, a p-value of less than 0.0001 and an F-value of 61.80 demonstrated the significance of the applied model. The high values of R^2 (0.9876), adj. R^2 (0.9716), and predicted R^2 (0.8011) indicate the appropriateness of the quadratic model in this study (Tables S5 and S6). The quadratic model shows significantly lower Akaike information criterion (AIC, 92.41) and Bayesian information criterion (BIC, 100.75) values than the linear (AIC 110.9, BIC 113.42) and two-factor interaction (2FI) models (AIC 107.11, BIC 112.94), indicating that it provides a better fit to the data without unnecessary model complexity. Furthermore, the variance inflation factor

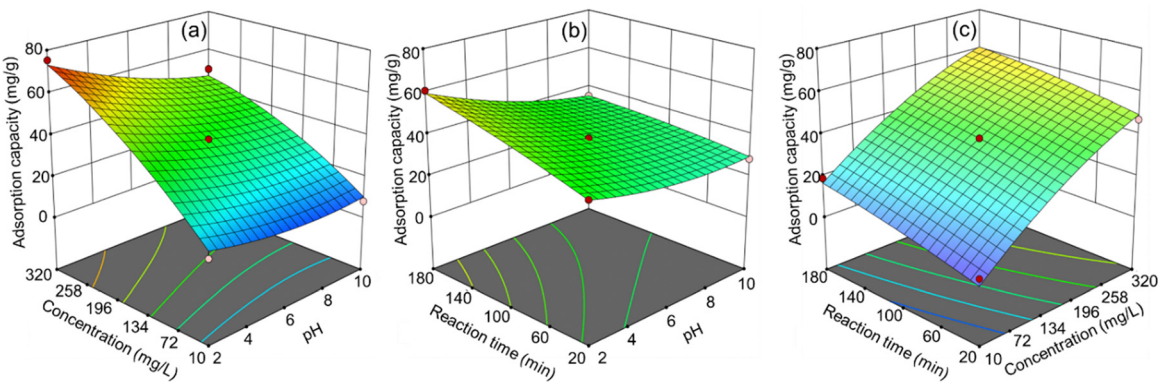

Fig. 10 The 3D response surface plots depicting Cr adsorption capacity as influenced by (a) pH and initial concentration (reaction time: 100 min), (b) pH and reaction time (concentration: 165 mg L^{-1}), and (c) reaction time and initial concentration (pH: 6).

(VIF) analysis confirmed the absence of multicollinearity (VIF $\sim$ 1 for all terms). According to the *F*-values, the influence of three variables on Cr adsorption capacity was ranked as initial concentration of Cr > pH > reaction time.

The 3D response surface diagram (Fig. 10) shows the combined effect of three factors. In Fig. 10(a), a significant increase in adsorption capacity is observed as the initial Cr concentration increased and the pH decreased. Maximum adsorption is achieved at low pH (= 2) and high concentration (>250 mg L^{-1}) due to enhanced electrostatic attraction between Cr ions and the adsorbent surface. This finding is consistent with the results of the batch experiment. According to Fig. 10(b), the Cr adsorption capacity is increased with prolonged reaction time and decreased pH. It is observed from Fig. 10(c) that the initial Cr concentration has a significant influence on the Cr adsorption capacity of CNT-CZB nanocomposite.

4. Conclusions

This study demonstrates the synthesis and optimization of CNT and Co–Zn ferrite nanoparticle modified WHB, showing promising performance in the removal of Cr from wastewater. The introduction of CNTs enhanced Cr adsorption capacity, whereas ferrite nanoparticles facilitate the easy magnetic separation of the adsorbent following adsorption. An adsorption capacity of approximately 81 mg g^{-1} is achieved using CNT-CZB as an adsorbent for the synthetic Cr(VI) solution, which increases to about 101 mg g^{-1} for the tannery wastewater due to the high concentration of Cr(III) in the latter. The improved performance of the CNT-CZB nanocomposite is attributed to its relatively large surface area (75.95 m^2 g^{-1}), mesoporous structure (pore diameter: 20.4 nm), and availability of functional groups. The Cr adsorption process is spontaneous, endothermic, and thermally favorable. Batch experiments reveal that the initial concentration of Cr and pH had a significant impact on the Cr removal, and these results were consistent with statistical analysis. Overall, this nanocomposite is a promising and sustainable material for Cr removal from wastewater, while also effectively utilizing the invasive water hyacinth.

Author contributions

M. Hedayet Ullah: conceptualization, methodology, data curation, formal analysis, investigation, writing – original draft, review & editing. Mohammad Jellur Rahman: formal analysis, writing – review & editing, supervision.

Conflicts of interest

The authors declare that they have no known competing financial interests or personal relationships that could have appeared to influence the work reported in this paper.

Data availability

The data supporting this article have been included in this published article and its supplementary information (SI). Supplementary information is available. See DOI: https://doi.org/10.1039/d6ma00330c.

Acknowledgements

The authors express sincere gratitude to the Bangladesh University of Engineering and Technology (BUET) for providing the necessary institutional support, laboratory facilities, and academic assistance for conducting this research.

References

1 N. Sheraz, A. Shah, A. Haleem and F. J. Iftikhar, Comprehensive assessment of carbon-, biomaterial- and inorganic-based adsorbents for the removal of the most hazardous heavy metal ions from wastewater, *RSC Adv.*, 2024, **14**, 11284–11310.
2 K. Jomova, S. Y. Alomar, E. Nepovimova, K. Kuca and M. Valko, Heavy metals: toxicity and human health effects, *Arch. Toxicol.*, 2025, **99**, 153–209.
3 S. Sharafi and F. Salehi, Comprehensive assessment of heavy metal (HMs) contamination and associated health risks in agricultural soils and groundwater proximal to industrial sites, *Sci. Rep.*, 2025, **15**, 7518.
4 N. R. Putra, M. A. A. Zaini, H. S. Kusuma, H. Darmokoesoemo and A. N. M. Faizal, Advances in chromium removal using biomass-derived activated carbon: A comprehensive review and bibliometric analysis, *Environ. Prog. Sustainable Energy*, 2025, **44**, 14598.
5 R. H. Pedroza, C. David, J. L. Barriada, C. Rey-Castro and P. Lodeiro, The role of photooxidation and organic matter in Cr(III) and Cr(VI) interactions with poly (lactic acid) microplastics in aqueous solution, *Sci. Total Environ.*, 2025, **963**, 178431.
6 A. Alshahrani, A. Alharbi, S. Alnasser, M. Almihdar, M. Alsuhybani and B. AlOtaibi, Enhanced heavy metals removal by a novel carbon nanotubes buckypaper membrane containing a mixture of two biopolymers: Chitosan and i-carrageenan, *Sep. Purif. Technol.*, 2021, **276**, 119300.
7 Y. Mei, S. Zhuang and J. Wang, Adsorption of heavy metals by biochar in aqueous solution: A review, *Sci. Total Environ.*, 2025, **968**, 178898.
8 A. Singh, S. S. Shah, C. Sharma, V. Gupta, A. K. Sundramoorthy, P. Kumar and S. Arya, An approach towards different techniques for detection of heavy metal ions and their removal from waste water, *J. Environ. Chem. Eng.*, 2024, **12**, 113032.
9 M. H. Ullah and M. J. Rahman, Adsorptive removal of toxic heavy metals from wastewater using water hyacinth and its biochar: A review, *Heliyon*, 2024, **10**, 36869.
10 M. Yaqub, L. Mee-Ngern and W. Lee, Cesium adsorption from an aqueous medium for environmental remediation: A

comprehensive analysis of adsorbents, sources, factors, models, challenges, and opportunities, *Sci. Total Environ.*, 2024, **950**, 175368.

11 A. M. Amin, H. A. Ibrahium, A. A. Gouda, R. E. Sheikh, B. M. Atia, M. A. Gado and N. S. Awwad, Design and utilisation of a novel poly imino-phosphorane composite for the effective removal of Pb^{2+} and Cr^{3+} ions from contaminated water sources, *Int. J. Environ. Anal. Chem.*, 2024, **105**(18), 1–28.

12 S. A. Mahmoud, B. M. Atia and M. A. Gado, Efficient removal of toxic metals (Hg(II), Cr(III), Pb(II), Cd(II)) using high-performance polyvinyl alcohol-L-2-Amino-3 mercaptopropionic acid composite from wastewater, *Int. J. Environ. Sci. Technol.*, 2025, **22**, 12269–12294.

13 Y. Yang, F. Sun, J. Li, J. Chen and M. Tang, The effects of different factors on the removal mechanism of Pb (ii) by biochar-supported carbon nanotube composites, *RSC Adv.*, 2020, **10**, 5988–5995.

14 M. Inyang, B. Gao, A. Zimmerman, M. Zhang and H. Chen, Synthesis, characterization, and dye sorption ability of carbon nanotube–biochar nanocomposites, *Chem. Eng. J.*, 2014, **236**, 39–46.

15 B. Yuan, S. Zhang, D. Ren and X. Zhang, Research progress on the removal of heavy metals in water and soil by modified carbon nanotubes: a review, *Water, Air, Soil Pollut.*, 2024, **235**, 418.

16 L. Wang, Y. Zhu, L. Ma, X. Hai, X. Li, Z. Yang, Y. Gao, M. Yuan, H. Xiong, M. Chen and X. Ma, Efficient removal of Chromium(VI) from wastewater based on magnetic multi-walled carbon nanotubes coupled with deep eutectic solvents, *Chemosphere*, 2024, **362**, 142732.

17 B. Ye, S.-I. Kim, M. Lee, M. Ezazi, H.-D. Kim, G. Kwon and D. H. Lee, Synthesis of oxygen functionalized carbon nanotubes and their application for selective catalytic reduction of NO_x with NH_3, *RSC Adv.*, 2020, **10**, 16700–16708.

18 M. J. Rahman and T. Mieno, Water-Dispersible Multiwalled Carbon Nanotubes Obtained from Citric- Acid-Assisted Oxygen Plasma Functionalization, *J. Nanomater.*, 2014, **2014**, 508192.

19 J. Hu, C. Chen, X. Zhu and X. Wang, Removal of chromium from aqueous solution by using oxidized multiwalled carbon nanotubes, *J. Hazard. Mater.*, 2009, **162**, 1542–1550.

20 Y. Trivedi, M. Sharma, R. K. Mishra, A. Sharma, J. Joshi, A. B. Gupta, B. Achintya, K. Shah and A. K. Vuppaladadiyamd, Biochar potential for pollutant removal during wastewater treatment: A comprehensive review of separation mechanisms, technological integration, and process analysis, *Desalination*, 2025, **600**, 118509.

21 E. Mosaffa, N. A. Ramsheh, D. Patel, M. Oroujzadeh and A. Banerjee, Textile industrial wastewater treatment using eco-friendly Kigelia fibrous biochar: Column and batch approaches, *Process Saf. Environ. Prot.*, 2025, **194**, 555–571.

22 M. Gado, M. Rashad, W. Kassab and M. Badran, Highly developed surface area thiosemicarbazide biochar derived from aloe vera for efficient adsorption of uranium, *Radiochemistry*, 2021, **63**(3), 353–363.

23 D. Nikhila Sri, R. Kottapalli, A. Pavani, C. Ganteda, E. Gouthami, A. Abd-Elmonem, S. A. Haroun, S. M. Hussain, M. Bayram and A. H. Almaliki, Comparison between response surface methodology and Taguchi method for dyeing process parameters optimization in fabric manufacturing by empirical planning, *Sci. Rep.*, 2025, **15**, 10209.

24 C. Munien, E. K. Tetteh and S. Rathilal, Response Surface Optimization of CuS Photocatalytic Process Using UV-vis Irradiation for Wastewater Treatment, *Energy Sci. Eng.*, 2025, **13**, 2922–2939.

25 M. H. Ullah and M. J. Rahman, Efficient Cr(VI) removal from tannery wastewater using Co–Zn ferrite-modified water hyacinth biochar: mechanisms and optimization, *Environ. Monit. Assess.*, 2025, **197**, 623.

26 X. Guo, A. Liu, J. Lu, X. Niu, M. Jiang, Y. Ma, X. Liu and M. Li, Adsorption mechanism of hexavalent chromium on biochar: kinetic, thermodynamic, and characterization studies, *ACS Omega*, 2020, **5**, 27323–27331.

27 Y. Ma, L. Yang, L. Wu, P. Li, X. Qi, L. He, S. Cui, Y. Ding and Z. Zhang, Carbon nanotube supported sludge biochar as an efficient adsorbent for low concentrations of sulfamethoxazole removal, *Sci. Total Environ.*, 2020, **718**, 137299.

28 D. D. Andhare, S. R. Patade, J. S. Kounsalye and K. Jadhav, Effect of Zn doping on structural, magnetic and optical properties of cobalt ferrite nanoparticles synthesized via. Co-precipitation method, *Phys. B*, 2020, **583**, 412051.

29 F. Wang, W. Sun, W. Pan and N. Xu, Adsorption of sulfamethoxazole and 17β-estradiol by carbon nanotubes/$CoFe_2O_4$ composites, *Chem. Eng. J.*, 2015, **274**, 17–29.

30 C. Ondijo, F. Kengara and I. K'Owino, Synthesis, Characterization, and Evaluation of the Remediation Activity of Cissus quadrangularis Zinc Oxide Nanoparticle-Activated Carbon Composite on Dieldrin in Aqueous Solution, *J. Nanotechnol.*, 2022, **2022**, 2055024.

31 S. Rao, M. Madhushree and K. S. Bhat, Characteristics of surface modified sugarcane bagasse cellulose: application of esterification and oxidation reactions, *Sci. Rep.*, 2024, **14**, 24136.

32 M. Ebrahimi Naghani, M. Neghabi, M. Zadsar and H. Abbastabar Ahangar, Synthesis and characterization of linear/nonlinear optical properties of graphene oxide and reduced graphene oxide-based zinc oxide nanocomposite, *Sci. Rep.*, 2023, **13**, 1496.

33 A. Osorio, I. Silveira, V. Bueno and C. Bergmann, H_2SO_4/HNO_3/HCl—Functionalization and its effect on dispersion of carbon nanotubes in aqueous media, *Appl. Surf. Sci.*, 2008, **255**, 2485–2489.

34 R. Suresh, Á. Álvarez, C. Sandoval, E. Ramírez, P. Santander, R. Mangalaraja and J. Yáñez, FeO_3/NiO nanocomposites: synthesis, characterization and roxarsone sensing by Fourier transform infrared photoacoustic spectroscopy, *New J. Chem.*, 2023, **47**, 12806–12815.

35 V. Vats, G. Melton, M. Islam and V. V. Krishnan, FTIR spectroscopy as a convenient tool for detectionand identification of airborne Cr(VI) compounds arising from arc welding fumes, *J. Hazard. Mater.*, 2023, **448**, 130862.

36 D. Zhu, J. Shao, Z. Li, H. Yang, S. Zhang and H. Chen, Nano nickel embedded in N-doped CNTs- supported porous biochar for adsorption-reduction of hexavalent chromium, *J. Hazard. Mater.*, 2021, **416**, 125693.

37 A. Lazzarini, A. Piovano, R. Pellegrini, G. Leofanti, G. Agostini, S. Rudić, M. R. Chierotti, R. Gobetto, A. Battiato, G. Spoto and A. Zecchina, A comprehensive approach to investigate the structural and surface properties of activated carbons and related Pd-based catalysts, *Catal. Sci. Technol.*, 2016, **6**(13), 4910–4922.

38 H. Murphy, P. Papakonstantinou and T. T. Okpalugo, Raman study of multiwalled carbon nanotubes functionalized with oxygen groups, *J. Vac. Sci. Technol., B*, 2006, **24**(2), 715–720.

39 A. M. Padhan, P. M. Rajaitha, S. Nayak, S. Hajra, M. Sahu, Z. Jagličić, P. Koželj and H. J. Kim, Synthesis and application of mixed-spinel magnesioferrite: structural, vibrational, magnetic, and electrochemical sensing properties, *Mater. Chem. Front.*, 2023, **7**(1), 72–84.

40 Y. Hao, H. Ma, Q. Wang, C. Zhu and A. He, Complexation behaviour and removal of organic-Cr(III) complexes from the environment: A review, *Ecotoxicol. Environ. Saf.*, 2022, **240**, 113676.

41 J. Wang and X. Guo, Rethinking of the intraparticle diffusion adsorption kinetics model: Interpretation, solving methods and applications, *Chemosphere*, 2022, **309**, 136732.

42 F. Jiang, C. Wei, Z. Yu, L. Ji, M. Liu, Q. Cao, L. Wu and F. Li, Fabrication of iron-containing biochar by on step ball milling for Cr(VI) and tetracycline removal from wastewater, *Langmuir*, 2023, **39**, 18958–18970.

43 S. R. Mishra, P. Roy, V. Gadore and M. Ahmaruzzamaan, A combined experimental and modeling approach to elucidate the adsorption mechanism for sustainable water treatment via In2S3-anchored chitosan, *Sci. Rep.*, 2023, **13**, 18051.

44 A. Sanchez-Hachair and A. Hofmann, Hexavalent chromium quantification in solution: Comparing direct UV–visible spectrometry with 1, 5-diphenylcarbazide colorimetry, *C. R. Chim.*, 2018, **21**(9), 890–896.

45 A. L. Petrou, V. Thoma and K. Tampouris, Kinetics and Mechanism of the Reaction between Chromium(III) and 2, 3-Dihydroxybenzoic Acid in Weak Acidic Aqueous Solutions, *Bioinorg. Chem. Appl.*, 2010, **2010**(1), 348692.

46 J. Geng, Y. Yin, Q. Liang, Z. Zhu and H. Luo, Polyethyleneimine cross-linked graphene oxide for removing hazardous hexavalent chromium: Adsorption performance and mechanism, *Chem. Eng. J.*, 2019, **361**, 1497–1510.

47 R. Juturu, R. Selvaraj and V. R. Murty, Efficient removal of hexavalent chromium from wastewater using a novel magnetic biochar composite adsorbent, *J. Water Proc. Eng.*, 2024, **66**, 105908.

48 J. Yan, Y. Wen and B. Feng, Efficient removal of hexavalent chromium using l-cysteine-modified chitosan with polyacrylamide in a one-step flocculation-precipitation process, *Results Eng.*, 2025, **27**, 106282.

49 S. A. Felemban, Utilization of chitosan/activated kaolinite nanocomposite based on shrimp shells for effective removal of hexavalent chromium ions: kinetic and thermodynamic studies, *Environ. Sci. Pollut. Res.*, 2025, **32**(33), 19740–19756.